Tectonophysics 666 (2016) 66–75

Contents lists available at ScienceDirect

Tectonophysics

journal homepage: www.elsevier.com/locate/tecto

Fault modeling of the 2012 Wutai, Taiwan earthquake and its tectonic implications

Pan-Hsin Chiang [a], Ya-Ju Hsu [a,*], Wu-Lung Chang [b]

[a] Institute of Earth Sciences, Academia Sinica, Taipei, Taiwan
[b] Department of Earth Sciences, National Central University, Chungli, Taiwan

ARTICLE INFO

Article history:
Received 23 December 2014
Received in revised form 28 September 2015
Accepted 13 October 2015
Available online 10 November 2015

Keywords:
Wutai earthquake
Coseismic slip distribution
GPS
Friction
Rheology

ABSTRACT

The M_w 5.9 Wutai earthquake of 26 February 2012 occurred at a depth of 26 km in southern Taiwan, where the rupture is not related to any known geologic structures. To illustrate the rupture source of the mainshock, we employ an elastic half-space model and GPS coseismic displacements to invert for optimal fault geometry and coseismic slip distribution. With observations of both coseismic horizontal and vertical displacements less than 10 mm, our preferred fault model strikes 312° and dips 30° to the northeast and exhibits a reverse slip of 28–112 mm and left-lateral slip of 9–45 mm. Estimated geodetic moment of the Wutai earthquake is 1.3×10^{18} N-m, equivalent to an M_w 6.0 earthquake. The Wutai epicentral area is characterized by a NE–SW compression as evidenced by the slaty cleavage orientations and the interpretation of stress tensor inversion of earthquake focal mechanisms. Using the stress drops of the Wutai and the nearby 2010 M_w 6.4 Jiashian earthquakes, we obtain a lower bound of ~0.002 for the coefficient of friction on the fault. On the other hand, studying the crustal thickness contrast in southern Taiwan provides an upper bound of the average horizontal compressive force of 1.67×10^{12} N/m transmitted through the Taiwan mountain belt and gives an estimate of the maximum friction coefficient for 0.03. The deviation of an order of magnitude difference between the upper and lower bounds for the coefficient of friction suggests that other fault systems may support substantial differential stress in the lithosphere as well.

1. Introduction

On February 26 2012, the Wutai M_w 5.9 earthquake occurred at a depth of 26 km in southern Taiwan. The centroid moment tensor solution from BATS (Broadband Array in Taiwan for Seismology) indicates a sinistral thrust mechanism that is similar to the focal mechanism of the March 4, 2010, Jiashian earthquake (M_w 6.4) (Hsu et al., 2011), located 25 km north of the Wutai mainshock (Fig. 1). These two ruptures trend NW–SE, which is inconsistent with the primary N–S trending structures associated with the plate convergence between the Eurasian plate and the Philippine Sea plate. The only known active fault in this area is the N–S trending and high-angle east-dipping Chaochou fault (Lewis et al., 2004) (Fig. 1) that, however, obviously does not correspond to the Wutai rupture. Since the Wutai mainshock occurred in a region with relatively low background seismicity (Hsu et al., 2011; Lee et al., 2013), the earthquake locations would not be able to illustrate the geometry of the unknown active faults. We first attempt to examine the orientations of the fault strikes by using the earthquake focal mechanisms prior to the Wutai mainshock and then discuss the relationship between the Wutai mainshock and the active structures in the adjacent area.

Estimates of surface strain rates based on GPS velocities (Hsu et al., 2011) show an E–W extension (Fig. 2), which correlates well with the abundant normal-faulting events at shallow depths (<10 km). However, the nearly vertical maximum compressive stress axis near the surface does not correspond with the NE–SW compressive stress axis at depths of 20–30 km inferred from the focal mechanisms of the Wutai and Jiashian earthquakes. Variations of the focal mechanism types at these depths may also reflect changes in azimuths and amplitudes of the principal stress axes. Here we use GPS coseismic displacements to infer the Wutai rupture model and examine surface strain rates as well as focal mechanisms with the intent of delineating the seismogenic features in this area. We then discuss the relationship between the coseismic slip pattern and the stress field as well as the rheology of the lithosphere in southern Taiwan.

2. Data collection and processing

Position time series of 25 continuous GPS (cGPS) stations near the epicenter of the Wutai earthquake were used to estimate coseismic surface displacements (Fig. 1). The cGPS data were collected by several organizations in Taiwan, including the Central Geological Survey (CGS),

* Corresponding author at: P.O. Box 1-55 Nankang, Taipei, Taiwan. Tel.: +886 2 27839910x415; fax: +886 2 2783 9871.

http://dx.doi.org/10.1016/j.tecto.2015.10.015

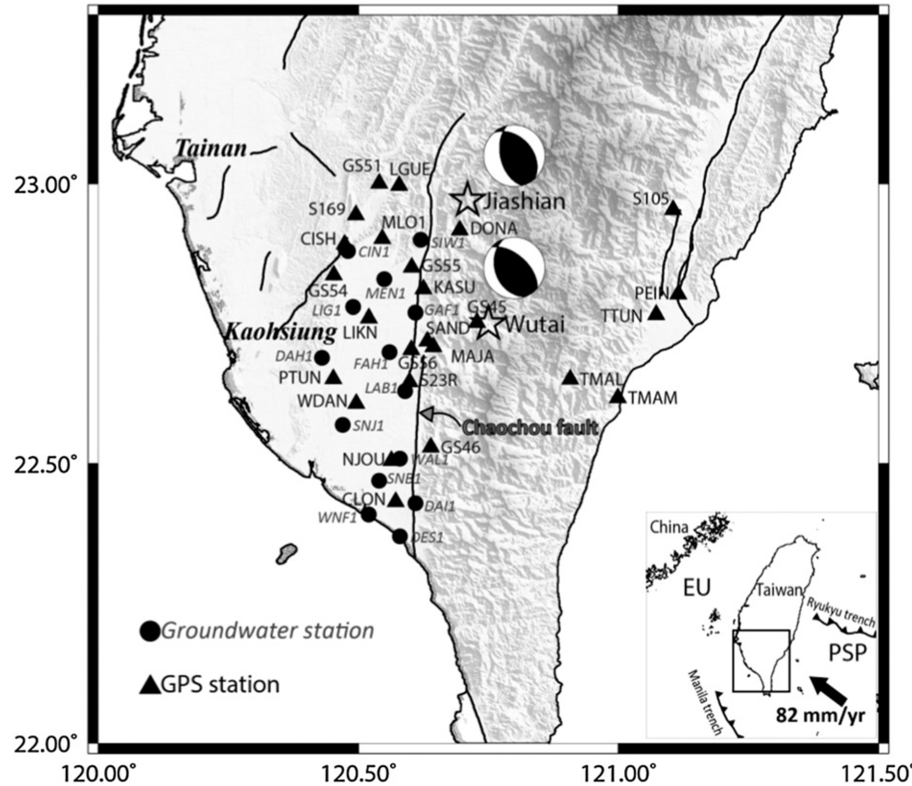

Fig. 1. Station distributions of the study area. Continuous GPS and groundwater well stations are denoted by triangles and circles, respectively. The star shows the epicenters of the Wutai and Jiashian earthquakes. Earthquake focal mechanisms of the Wutai and Jiashian earthquakes are from BATS (http://bats.earth.sinica.edu.tw/). Black lines show major active faults. The known active fault closest to the Wutai epicenter is the N–S trending Chaochou fault. Topography is shown as shaded relief. Inset shows the regional tectonics with the bold arrow indicating the plate convergence between the Eurasian plate (EU) and the Philippine Sea plate (PSP) (Yu et al., 1997).

the Institute of Earth Sciences, Academia Sinica (IESAS), the Ministry of Interior Affairs (MOI), and the Central Weather Bureau (CWB). We processed data using the GAMIT/GLOBK software to obtain three-dimensional daily coordinates of stations in the International Terrestrial Reference Frame 2005 (ITRF05). All cGPS sites used here were operated for periods of 2–12 years before the Wutai mainshock. We used a least-square method to fit the position time series with a function combining a linear term, periodic motions, offsets due to earthquakes or equipment malfunctions (Williams, 2003), and postseismic relaxation of large earthquakes (Eq. (1)) (Nikolaidis, 2002),

$$y(t_i) = a + bt_i + c\sin\left(\frac{2\pi}{p}t_i\right) + d\cos\left(\frac{2\pi}{p}t_i\right) + \sum_{j=1}^{n_g} g_{\boldsymbol{j}}\boldsymbol{H}(t_i - T_{gj}) + \sum_{j=1}^{n_k} k_{\boldsymbol{j}}\exp\left(-\frac{t_i - T_{kj}}{\tau_j}\right)H(t_i - T_{kj}) + \nu_{\boldsymbol{i}} \quad (1)$$

where t_i ($i = 1 \ldots N$) is time in units of day; a and b are the intercept and the amplitude of the linear trend; and c and d are the amplitudes of sinusoidal periodic motions, with p representing the period. $\boldsymbol{H}(\boldsymbol{t})$ is the Heaviside step function, with term g_j indicating the magnitude of coordinate offset at epochs T_g. Postseismic motion is modeled as an exponential decay with magnitudes k following earthquakes at epochs T_k and τ estimated empirically. The value ν indicates residuals.

Previous studies have shown that GPS position time series are influenced by the seasonality of hydrological loading (Blewitt and Lavallée, 2002; van Dam et al., 2001), especially in the vertical component (Dong et al., 2002). We employ the Fast Fourier Transform (FFT) to evaluate the dominant periods of periodic signals in GPS data (Fig. 3a) and compare the results with those of ground water level records collected by the Water Resources Agency (WRA), Taiwan Ministry of Economic Affairs (Fig. 3b). The power spectra of GPS position time series and ground water levels both show high energy at frequencies of ~1 and 2 cycle/year, which suggests significant annual and semi-annual modulations of ground water level variations on GPS data (Fig. 3c). Therefore, we consider two periodic motions (p equal to 1 and 0.5) in the linear regression (Eq. (1) and Fig. 3d).

The coseismic displacements of the Wutai earthquake are estimated from the amplitude of the Heaviside step function at the time of the mainshock (coefficient g in Eq. (1)), with the uncertainties of coseismic displacements calculated from the model covariance matrix as follows:

$$\sum\hat{\boldsymbol{x}} = \left(\boldsymbol{A}^{\boldsymbol{T}}\sum\nolimits_b^{-1}\boldsymbol{A}\right)^{-1} \quad (2)$$

where matrix $\boldsymbol{A}$ represents the model Green's function in the linear regression (Eq. (1)), and $\sum_b^{-1}$ is the covariance matrix of GPS observational error.

Table 1 lists the estimates and variances of coseismic surface displacements of the 2012 Wutai earthquake. The amplitudes of both horizontal and vertical displacements are less than 10 mm (Fig. 4), with the horizontal motions of 1–7 mm directed primarily to the west and southwest (Fig. 4a). The largest SW motion of 7.6 mm is observed at site GS56 located to the west of the epicenter. Coseismic vertical displacements show predominately near-field uplift and far-field subsidence. The amplitudes of vertical displacements are in a range of −5 to 8 mm with standard deviations of 3–10 mm (Fig. 4b).

3. Modeling of fault geometry and slip distribution

We use an elastic half-space dislocation model (Okada, 1985) and GPS coseismic displacements (Table 1) to invert for the optimal fault geometry and the slip distribution of the Wutai earthquake. Since the Wutai earthquake did not rupture to the surface, the focal mechanisms

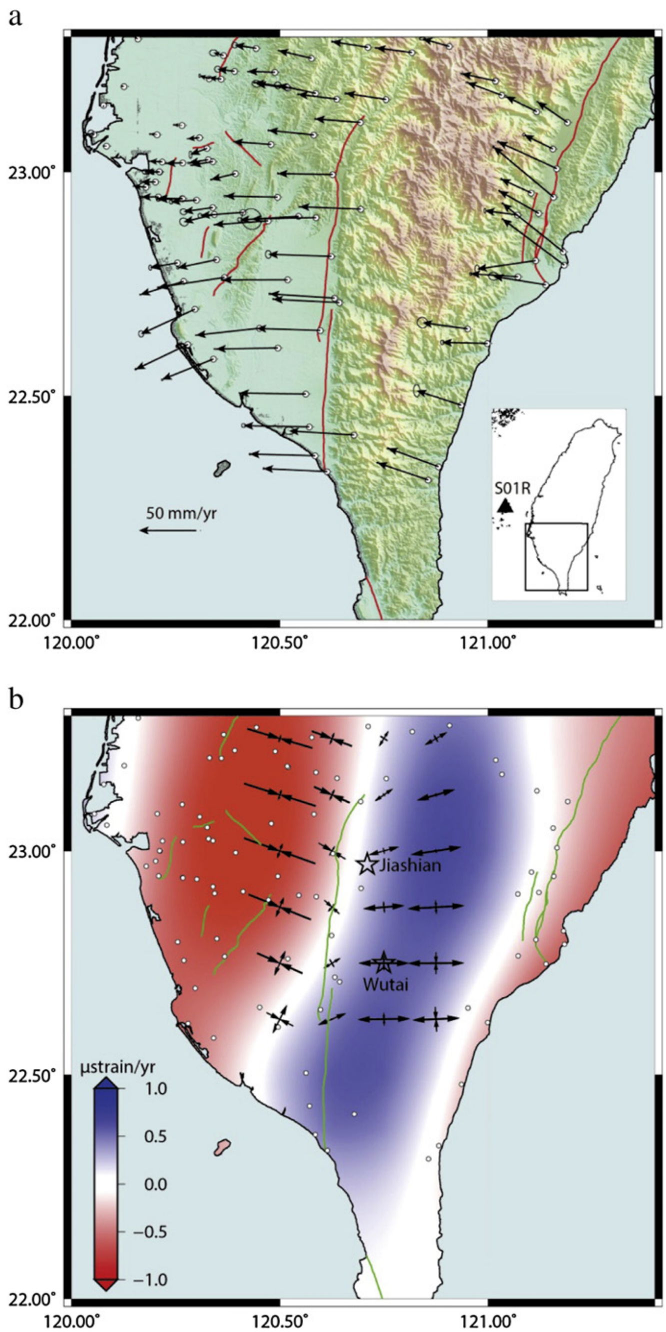

Fig. 2. (a) Horizontal velocities observed by GPS from 2005 to 2009 in southern Taiwan. Black arrows show velocities with respect to S01R (see inset) and the 95% confidence ellipses. Red lines indicate major faults. (b) Dilatation (background color) and principal strain rates (black arrows) are estimated from GPS velocities in (a). The stars show the epicenters of the Wutai and Jiashian earthquakes. Major faults are shown as green lines (GPS data from Hsu et al., 2011).

of the mainshock from BATS, RMT, GCMT and USGS as well as the aftershock distribution (Fig. 4) are used to provide a priori constrains for fault geometries. We employ a weighted least-square inversion algorithm to minimize the following misfit function:

$$\mathrm{F}(\mathrm{s},\beta,\mathbf{m}) = \|\Sigma^{-1/2}(\boldsymbol{G}(\boldsymbol{m})\mathbf{s}-\mathbf{d})\|^2 + \beta^{-2}\|\boldsymbol{\nabla}^2\boldsymbol{s}\|^2 \tag{3}$$

where $\Sigma^{-1/2}$ is the inverse of the square root of the data covariance matrix; $\boldsymbol{G}(\boldsymbol{m})$ is the Green's function of an elastic half-space, yielding 3-component displacements at any location resulting from unit slip on the fault (Okada, 1985); s is the slip, d is the observed coseismic displacement, and $\boldsymbol{\nabla}^2$ is a Laplacian smoothing operator with the smoothing parameter β determined by the trade-off curve between model roughness and data misfit (Harris and Segall, 1987). To evaluate the goodness of fit, we use the reduced chi-square defined as

$$\chi_r^2 = \frac{\sum_{i=1}^{N} {(O_i-P_i)^2}\Big/{\sigma_i{}^2}}{N} \tag{4}$$

where N is the total number of stations; O_i and P_i indicate observed and predicted displacements, respectively; and σ_i is the standard deviation of the observation. A value of 1 for χ_r^2 indicates that the model fits data acceptably well within data uncertainties.

We first calculate fault slip distribution using coseismic GPS displacements and a constant–slip rectangular fault plane. Since the Wutai rupture is related to a blind fault, we try both nodal planes constrained by earthquake focal mechanisms (Fig. 4b). We apply a grid-search inversion to find the optimal fault parameters (fault length, width, strike, dip, depth, position) and fault slip components (dip–slip and strike–slip) that minimize the Eq. (3). The N–S trending and west-dipping nodal plane gives a χ_r^2 value of 2.0 larger than the value of 1.4 for the NW–SE trending and NE-dipping nodal plane. Our coseismic slip inversion based on GPS data therefore indicates the NE-dipping nodal plane as the fault rupture plane. Furthermore, an average finite-rupture model by fitting synthetic and recorded broadband waveforms of the Wutai earthquake also suggested the NE-dipping rupture plane (Hsieh et al., 2014), in agreement with our results.

We search for fault parameters with different ranges based on a priori information from geologic and seismic evidence. The top depth of fault ranges from 1 to 40 km with an interval of 0.5 km, and distances between the middle point of the fault top and the epicenter range from −10 to 10 km with an interval of 1 km. The fault length and width range from 5 to 70 km with an interval of 5 km. Fig. 5a show a wide range of fault rupture size from 10 km by 10 km to 40 km by 50 km can give a satisfactory fit to GPS data. To estimate uncertainties of fault parameters, we calculate χ_r^2 in a total of 34,839 sets of fault parameters and choose the smallest ten percent of χ_r^2 to examine uncertainties and trade-offs between parameters (Fig. 5b). Histograms of the best 10% of fault parameters, for example, fault top depths and fault positions, are shown in Fig. 5c and d–e, respectively. The optimal solution of fault top depth is 18 km with uncertainties of 13–40 km (Fig. 5c); for fault position in the east direction, −3 km with uncertainties of −4 to 10 km (Fig. 5d); and for fault position in the north direction, 1 km with uncertainties of −3 to 6 km (Table 2) (Fig. 5e). Additionally, we plot the contours of χ_r^2 between different fault parameters (Fig. 5f–g). A linear trend is shown between the fault depth and the fault position, especially in the east direction, suggesting a strong trade-off between these parameters. In addition, we calculate the stress drop of the best 10% of fault parameters using the stress drop and moment relation for a circular fault model (Madariaga, 1979). Note that the stress drop is estimated by only choosing subfaults with slip greater than 80 mm. Estimates of stress drops are within a range from 1.0 to 1.3 MPa (Fig. 5h), consistent with the optimal result of 1.1 MPa.

Our preferred fault model with a uniform–slip rectangular fault plane has the χ_r^2 value of 1.0 and the average residual of 1.9 mm. The fault dimension is 24 km in length and 15 km in width, extending from 18 to 25.5 km at depths. The fault strikes 312° and dips 30° to northeast. To account for spatial variation of fault slip, we divide the fault plan into 25 patches and estimate the coseismic slip on each fault patch by fixing the above fault geometry and position. We impose thrust and left-lateral slip directions to ensure that the slip pattern would be consistent with the coseismic surface displacements. The preferred slip model with multiple fault patches gives a χ_r^2 value of 1.1, indicating that the model fits the GPS observations within data uncertainties with the average residuals in east, north, and vertical components of about

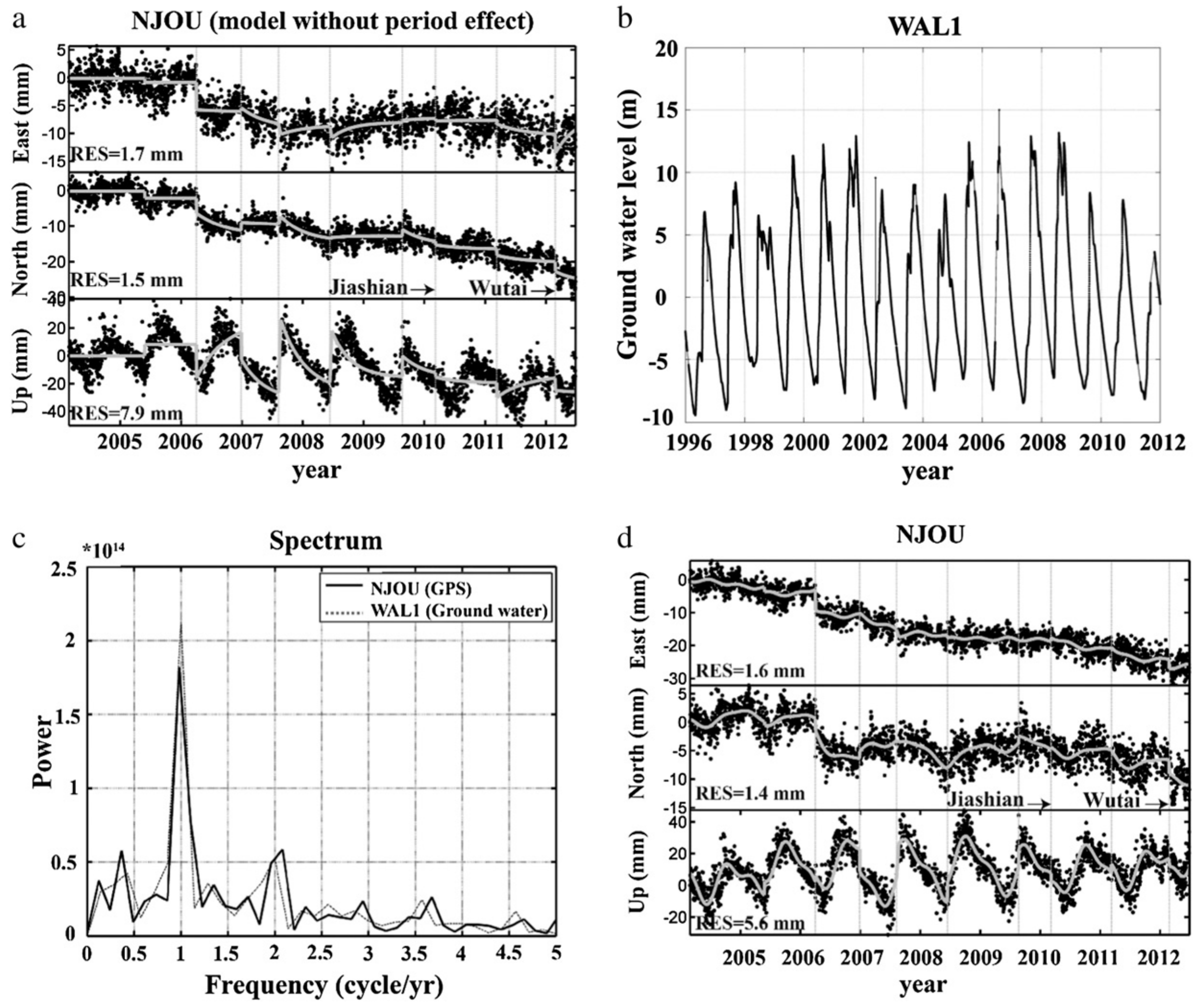

Fig. 3. (a) Position time series of GPS station NJOU, from top to bottom are the east, north, and vertical components. Dots and lines show observations and model fits based on the Eq. (1). Vertical lines indicate the times of earthquakes ($M_w > 5$). Average residual of each component (RES) is shown as black text. Note that the model fit does not include the periodic fluctuations of groundwater table. (b) The temporal variations of ground water levels at site WAL1, located about 2 km to the east of the GPS site NJOU. (c) Power spectrums of GPS vertical time series at site NJOU and ground water levels at site WAL1 are shown as solid-black and gray-dash lines, respectively. The amplitude of the power spectrum of ground water level is divided by ten. (d) Similar to (a), but the model takes account the groundwater effect.

1.7, 1.1 and 3.0 mm, respectively (Fig. 6). We notice that the predicted coseismic GPS displacements at few GPS sites to the SW of the earthquake are under-predicted by large amounts, which may be associated with un-modeled site effects due to deep unconsolidated sediments in the Pingtung Plain.

4. Inversion results and tectonics implications

The coseismic slip distribution exhibits a reverse motion of 28–112 mm and a left-lateral motion of 9–45 mm. The largest slip of 121 mm is located at a depth range of 20–25 km at the western side of the epicenter (Fig. 6). Given a shear modulus of 50 GPa, the geodetic moment of the Wutai earthquake is 1.3×10^{18} N-m, equivalent to an M_w 6.0 earthquake that is slightly larger than the seismic moments of 1.5×10^{17} and 1×10^{18} N-m determined by BATS and GCMT respectively. This discrepancy between the geodetic and seismic moments may be due to additional surface displacements resulted from early aftershocks or the postseismic deformation.

The NW–SE trending of the 2012 Wutai earthquake rupture is inconsistent with the primary N–S trending geologic structures, for instance, the Chaochou fault. The N–S trending, east-dipping, and high-angle Chaochou fault is the only known active fault near the Wutai hypocentral region (Fig. 6). Wiltschko et al. (2010) studied the characteristics of the slaty cleavages along the Chaochou fault and found that in-situ measurements of bedding and foliation strike NE and dip to the SE in the northern and southern Chaochou fault, suggesting a NW–SE compression. However, the bedding and foliation in the middle section mainly strikes NW implying a NE–SW compression, consistent with the coseismic slip pattern of the Wutai mainshock. In addition, stress tensor inversions from earthquake focal mechanisms (Rau et al., 2012) show that the NE-trending σ_1 axes are located near the Jiashian rupture zone. The orientations of σ_1 axes differ from the pervasive orogen-perpendicular directions of σ_1 axes that are associated with the plate convergence in the neighboring regions.

According to the geological evidence and background seismicity, the stress regime near the Wutai earthquake shows a NE–SW compression, which is similar to the stress state near the 2010 Jiashian rupture area but different from the NW-trending compression in the vicinity. Chan and Wu (2012) calculated a coulomb stress change of ~0.2 bars imparted by the 2010 Jiashian earthquake near the 2012 Wutai epicenter and suggested that it may encourage the Wutai rupture. It appears that both the Wutai and Jiashian earthquakes resulted from a regional NE–SW compressional stress. Neither the 2012 Wutai nor the 2010 Jiashian earthquake rupture extended to the surface. The nearly north–south striking Chaochou fault (Fig. 6) is unlikely to be the causative faults of these two earthquakes. We analyze trends of strike–slip

Table 1
GPS station coordinates and coseismic displacements and uncertainties of the Wutai earthquake used in this study.

Site	Longitude (°)	Latitude (°)	D_E (mm)	D_N (mm)	D_U (mm)
CLON	120.5796	22.4301	−2.3 ± 1.6	−1.2 ± 1.4	−5.0 ± 4.8
GS45	120.7361	22.7508	−2.4 ± 1.4	−1.0 ± 1.2	5.9 ± 4.5
GS46	120.6475	22.5279	−2.6 ± 1.5	−2.4 ± 1.4	4.1 ± 5.5
GS51	120.5481	22.9985	−1.0 ± 1.6	1.1 ± 0.9	7.2 ± 5.0
GS54	120.4602	22.8354	−3.5 ± 1.1	0.4 ± 0.9	8.3 ± 5.7
GS55	120.6103	22.8489	−3.4 ± 1.4	3.8 ± 1.2	3.3 ± 4.0
GS56	120.6098	22.7021	−7.6 ± 2.1	−1.1 ± 1.8	0.5 ± 6.3
KASU	120.6330	22.8102	−4.5 ± 1.5	4.9 ± 1.3	4.3 ± 4.6
LGUE	120.6354	22.9929	−2.6 ± 1.9	−0.9 ± 1.5	−2.5 ± 7.7
LIKN	120.5279	22.7586	−4.8 ± 1.9	0.2 ± 1.6	3.4 ± 7.9
MAJA	120.6521	22.7076	−5.3 ± 1.1	−2.8 ± 0.9	6.4 ± 3.2
NJOU	120.5714	22.5039	−2.3 ± 1.8	−1.9 ± 1.0	3.7 ± 8.7
PTUN	120.4597	22.6499	−1.5 ± 2.2	−1.3 ± 1.8	4.3 ± 8.7
S23R	120.6062	22.6450	−3.9 ± 1.2	−3.1 ± 1.0	2.6 ± 3.7
S105	121.1129	22.9517	−2.9 ± 2.9	−1.6 ± 2.3	−1.3 ± 3.6
S169	120.5033	22.9423	−4.0 ± 1.4	−0.9 ± 1.5	1.9 ± 6.9
SAND	120.6406	22.7173	−4.2 ± 1.2	−2.5 ± 1.0	2.9 ± 3.6
TMAL	120.9599	22.6489	−2.7 ± 3.2 s	1.8 ± 2.1	−2.5 ± 7.3
TTUN	121.0807	22.7646	−3.5 ± 3.6	0.3 ± 2.0	1.4 ± 10.0
WDAN	120.5043	22.6061	−3.8 ± 1.1	−2.2 ± 1.3	4.8 ± 3.7
CISH	120.4812	22.8896	−3.2 ± 1.2	1.5 ± 1.0	3.0 ± 3.4
DONA	120.7035	22.9156	−2.3 ± 1.1	1.0 ± 1.0	1.1 ± 3.3
MLO1	120.5538	22.9000	−3.5 ± 1.2	1.9 ± 1.0	2.5 ± 3.8
PEIN	121.1231	22.8011	−2.9 ± 2.5	1.5 ± 0.9	1.0 ± 7.7
TMAM	121.0075	22.6161	−1.4 ± 3.1	−0.2 ± 2.1	4.4 ± 6.3

and thrust faulting earthquakes in this region using earthquake focal mechanisms from Wu et al. (2008). The location errors for earthquake focal mechanisms in longitude, latitude and depth are approximately 3 km, 1 km and 5 km, respectively (Wu et al., 2013). A total of 78 events with magnitudes from 3 to 6 occurred over the past two decades. The rose diagrams (Fig. 7) show that the majority of these earthquakes strike N–S and NE–SW, consistent with the surface geology, but different from the NW–SE trending fault strikes of the Wutai and Jiashian earthquakes.

Various focal mechanism types at different depths provide a good constraint to evaluate the transient depths of differential stress states. Normal-faulting earthquakes are characterized by nearly vertical maximum compressional stress axes (σ_1), whereas reverse-faulting earthquakes exhibit horizontal compressional stress axes. According to the theory of stress permutation (Angelier et al., 1985; Hu and Angelier, 2004), different focal mechanism types can exist in the same region when stress magnitudes are similar. In the compressional plate boundary, for example, switching between the σ_2 and σ_3 axes in depth will result in both reverse and strike–slip faulting events when these stresses have similar magnitudes. In contrast, switching between σ_1 and σ_2 axes in the extensional stress regime will cause normal and strike–slip faulting earthquakes.

The above features can be used to explain our observations of changes of focal mechanisms from the shallow to deep crust in southern Taiwan. To examine the transition depths where the switching of stress axes occurs, we plot the numbers of the normal-faulting, thrust-faulting, and strike–slip faulting events at different depths from 0 to 50 km in the study region (Fig. 8). We find normal-faulting events occur predominately at depths less than 10–15 km and thrust-faulting events occur mostly at depths below 15 km. The appearance of strike–slip faulting, however, is about the same at all depths. This suggests that the magnitudes of σ_1 and σ_2 stresses are similar at depths less than 10–15 km, while magnitudes of σ_2 and σ_3 are similar at depths below 15 km.

5. Implications for lithospheric rheology beneath the southern Central Range

Using the stress drop and moment relation for a circular fault model (Madariaga, 1979), we calculate the stress drop of 1.1 MPa

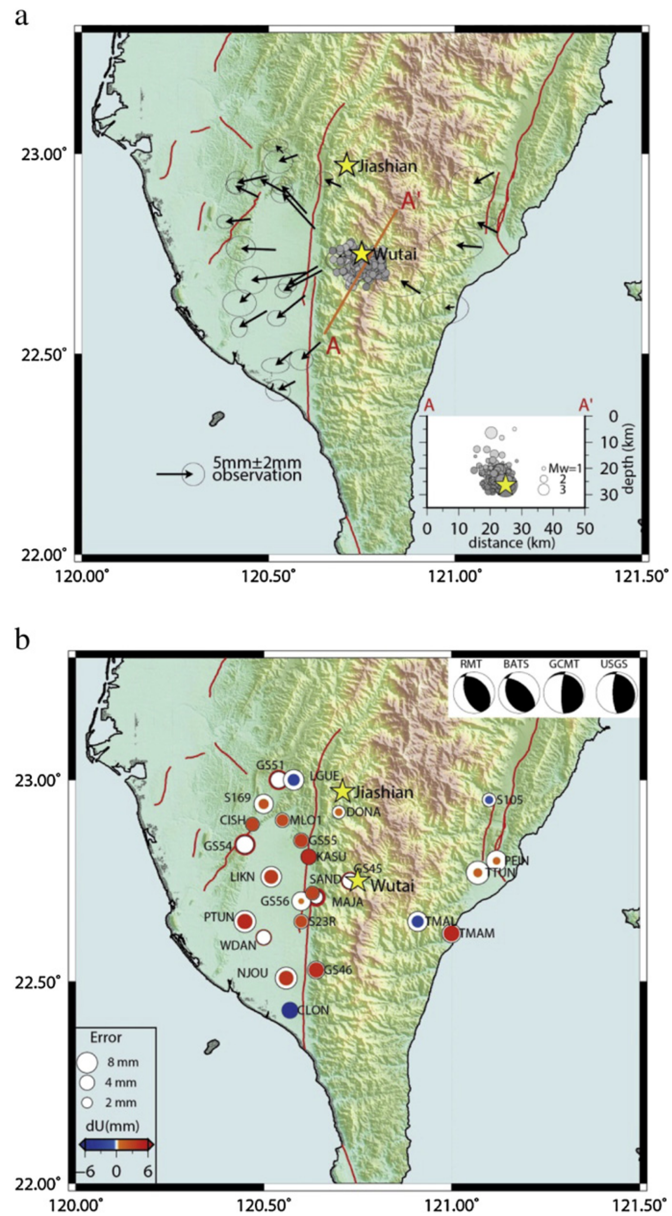

Fig. 4. Coseismic displacements of the Wutai earthquake (see Table. 1). (a) Black vectors show horizontal displacements with 68% confidence ellipses. The yellow stars show the epicenters of the Wutai and Jiashian earthquakes. Aftershocks following the Wutai earthquake are denoted by gray circles. A NE–SW cross-section of aftershocks (A–A′) is shown on the bottom right. (b) Vertical displacements are shown by circles, with uplift and subsidence indicated by red and blue colors, respectively. The white circle indicates one standard deviation. Focal mechanism of the mainshock from BATS, RMT (http://rmt.earth.sinica.edu.tw/), GCMT (http://www.globalcmt.org/CMTsearch.html) and USGS (http://www.usgs.gov/) are shown on the top right.

on the Wutai rupture plane, similar to the estimate of 1.0 MPa from the seismic waveform inversion (Shiann-Jong Lee, personal communication). Assuming that the Wutai earthquake releases all the shear stress on the fault plane, we can estimate the minimum coefficient of friction on the fault plane by the ratio of the shear stress (τ) to normal stress (σ_n) following the same method proposed by Copley et al. (2011). This estimate of the coefficient of friction (μ) is a lower bound because it is possible not all of the shear stresses were released in the earthquake. The value of μ is calculated by the following equations:

$$\tau = -\frac{\Delta\sigma_{xx}}{2}\sin 2\theta \qquad (5)$$

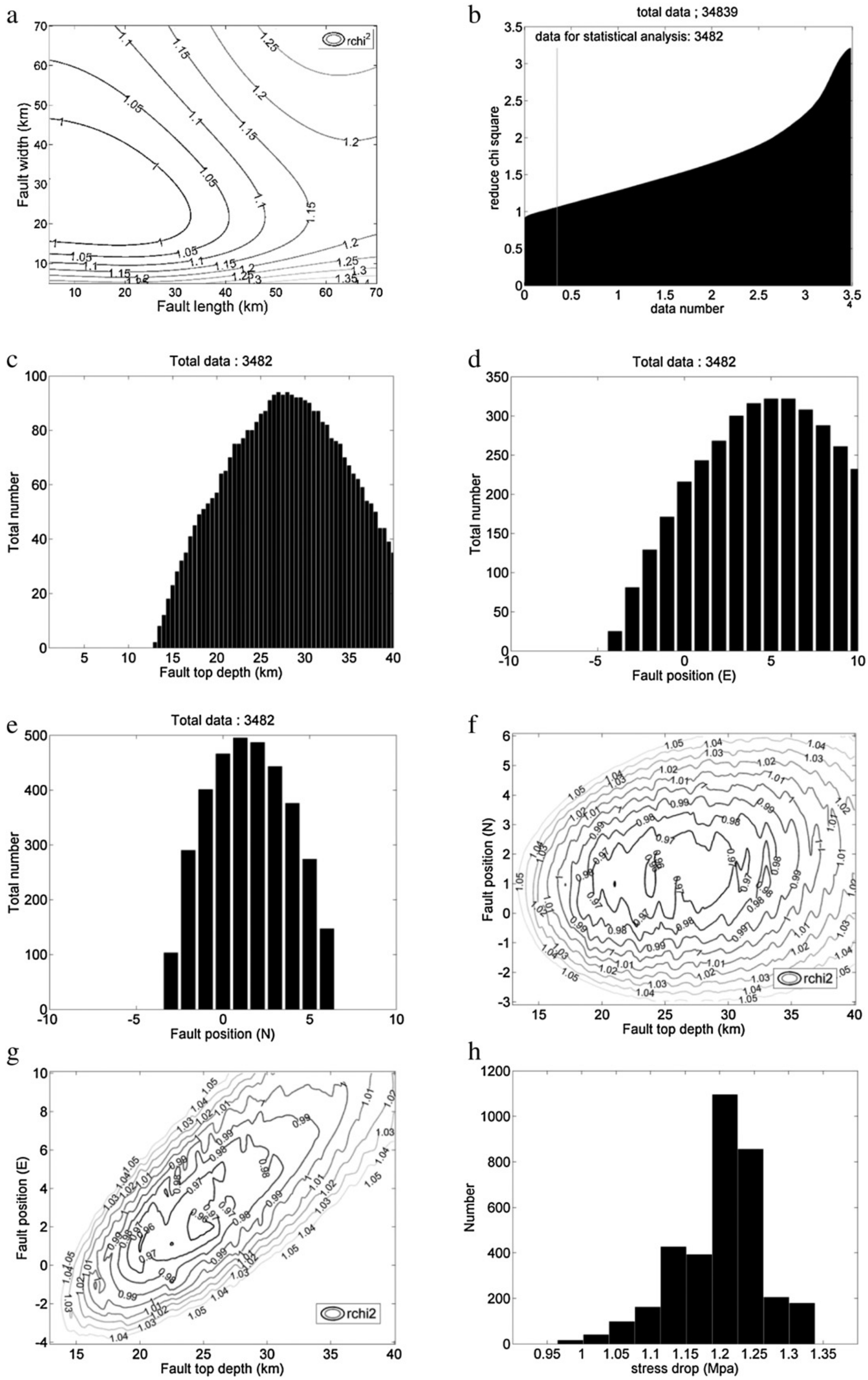

Fig. 5. Statistical analyses of fault parameters for a uniform slip model. (a) The correlation between fault length and fault width. The contours indicate the values of χ_r^2. (b) The histogram of χ_r^2 for all 34,839 fault models with different combinations of fault parameters. The gray line indicates the top 10% of the smallest values of χ_r^2. The histograms of the top 10% of the best-fit fault top depth, fault position in the east and west directions are shown in (c), (d), and (e), respectively. The correlations between the fault depth and the fault position in the north and east directions are shown in (f) and (g), respectively. The contours in (f) and (g) indicate the value of χ_r^2. (h) The histogram of stress drop for top 10% of the smallest values of χ_r^2.

Table 2
Optimal fault parameters and uncertainties for the Wutai coseismic slip model.

	Depth (km)	Position (km)	Length (km)	Width (km)	Strike (°)	Dip (°)
Value	18 (13–40)	E: −3 (−4 to 10) N:1 (−3 to 6)	24 (10–45)	15 (10–50)	312 (280–330)	30 (15–35)

$$\sigma_n = \rho g h + \frac{\Delta\sigma_{xx}}{2}(1 + \cos 2\theta) \quad (6)$$

$$\mu = \frac{\tau}{\sigma_n} \quad (7)$$

where $\Delta\sigma_{xx}$ is the horizontal differential stress, θ is the angle of the fault with respect to the vertical, ρ is the crustal density, g is the gravitational acceleration, and h is the depth (Turcotte and Schubert, 2002). We estimate the coefficient of friction, $\mu \geq 0.002$ for the rupture plane of the Wutai earthquake. Following the same method, we obtain a similar value for μ of 0.002 for the 2010 Jiashian earthquake by taking the stress drop of 1.2 MPa and the centroid depth of 25 km based on the seismic waveform inversion (Lee et al., 2013). Estimates of the lower-bound μ from these two earthquakes are compatible and may be representative for the seismogenic behavior in the mid-crust of the southern Central Range.

To evaluate the upper bound of μ, moreover, we first estimate the maximum horizontal compressive force constrained by the crustal thickness contrasts. If mountains undergo crustal extension on the top, then the vertical stress as a function of depth beneath the mountains can be used to define an upper bound of the horizontal driving force per unit length (Molnar and Lyon-Caen, 1988):

$$F = \rho_c g h\left(\frac{h}{2} + H_0 + \frac{\Delta H}{2}\right) \quad (8)$$

where ρ_c is the density of the crust, h is the elevation, H_0 is the crustal thickness, and ΔH is the thickness of the crustal root (Fig. 9a). Given $H_0 = 30$ km and $\Delta H = 10$ km and assuming no significant mechanical layering at depths <25 km based on seismic tomography of Vp and Vp/Vs (Kuo-Chen et al., 2012a,b), we estimate the maximum average horizontal force of 1.67×10^{12} N/m that corresponds to a horizontal compressive stress of 41.8 MPa for the southern Central Range. With this value and applying the Eqs. (5)–(7), we estimate the shear and normal stresses of 18.1 MPa and 559.3 MPa, respectively, on fault planes at the mid-depth of the seismogenic zone (20 km). Assuming the crust supports the differential stress of the lithosphere, the maximum value of μ is 0.03 for surfaces with the same dip (~35°) of the Wutai and Jiashian ruptures. Note that significant crustal bending due to horizontal

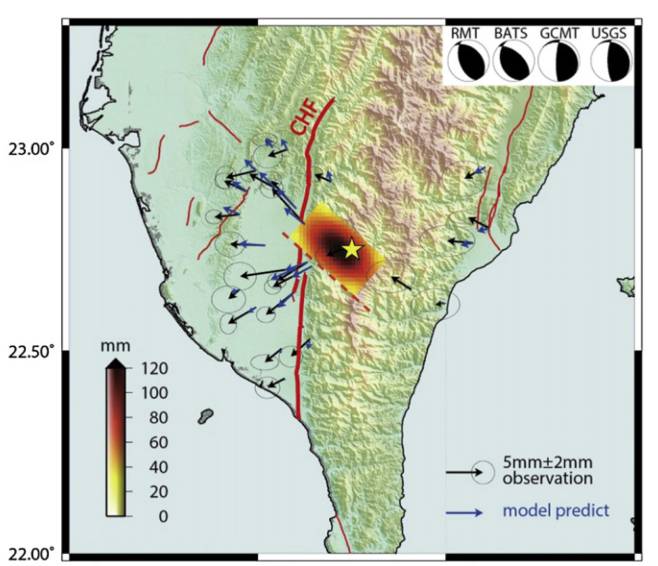

Fig. 6. Our best-fit coseismic fault model of the Wutai earthquake. GPS coseismic displacements with 68% confidence ellipses and modeled horizontal displacements are shown as black and blue vectors, respectively. Coseismic fault slip model projected to the surface is shown in color. Red dashed line indicates the top fault plane. The earthquake epicenter is shown as the yellow star. Four mainshock focal mechanisms on the top right are from BATS, RMT, GCMT and USGS, respectively. The bold red line indicates the Chaochou fault.

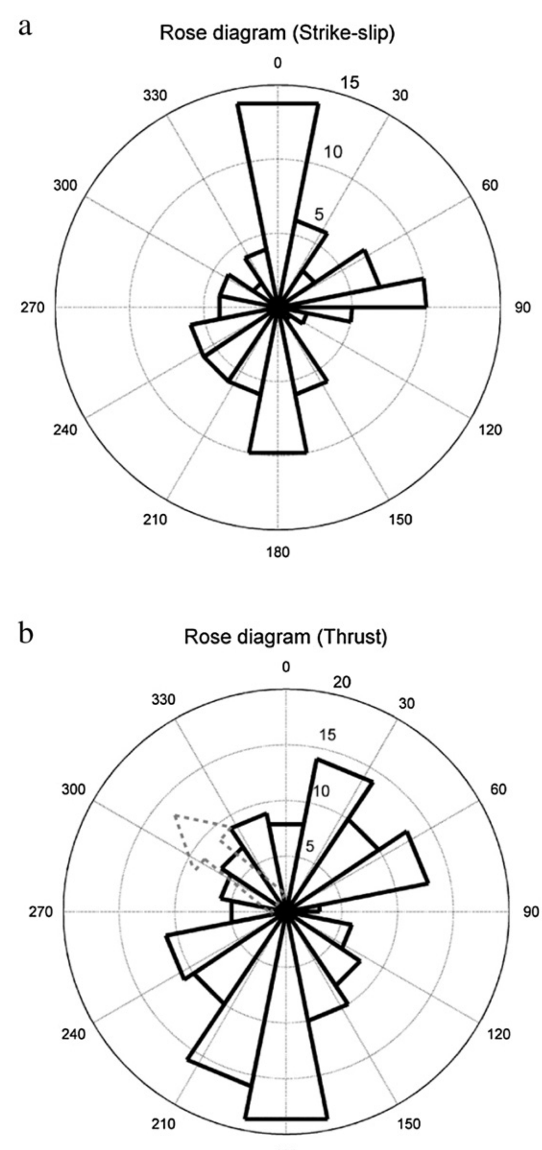

Fig. 7. Rose diagrams display distributions of fault strikes of two nodal planes constrained by earthquake focal mechanisms. (a) Strike–slip faulting earthquakes. (b) Thrust-faulting earthquakes. Earthquake catalog spans in the time period of 1990–2010 with magnitudes between 3 and 6. The dashed arrow in (b) indicates the strike of the Wutai earthquake.

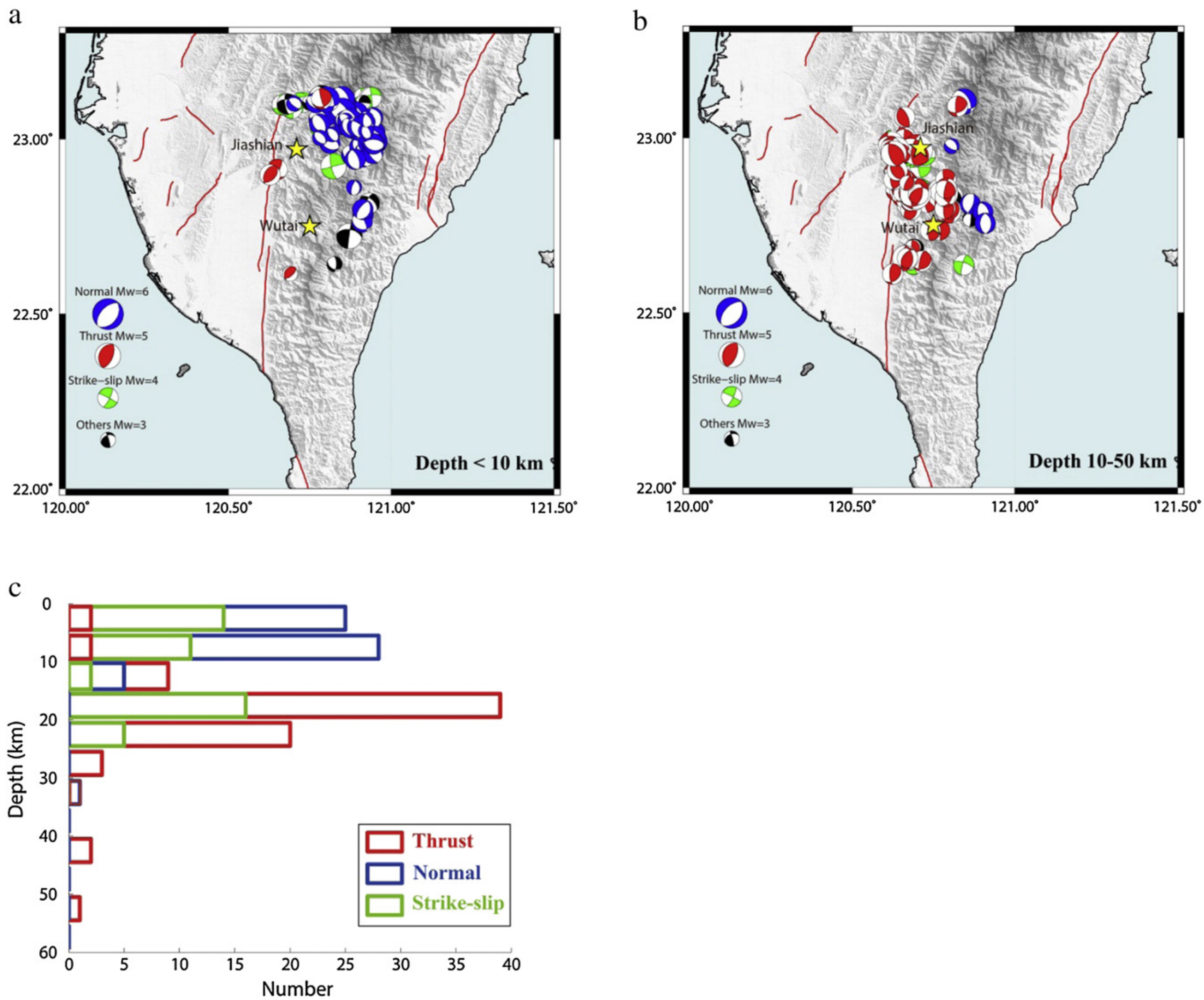

Fig. 8. Earthquake focal mechanisms at different depths prior to the Wutai earthquake in southern Taiwan: (a) less than 10 km, (b) from 10 to 50 km. (c) Depth distribution of different types of focal mechanism. Earthquake catalog spans in the time period of 1990–2010 with magnitudes from 3 to 6. The majority of the normal-faulting and thrust-faulting earthquakes are located at depths less than 10 km and greater than 15 km, respectively.

tectonic forces can affect the above results; however, Lin and Watts (2002) asserted that vertical loading can well explain the lithospheric flecture of western Taiwan. We thus consider crustal thickening instead of bending to be the major effect of horizontal compressive stress in the Central Range.

The lower bound of the coefficient of friction, inferred by the stress releases of the Wutai and Jiashian earthquakes, is an order of magnitude lower than the upper bound. The very low value of 0.002 may imply that the two earthquakes are not representative of the accumulated stress within the entire seismogenic crust, and the faults in the southern Central Range may not be able to support the entire stress transmitted through the mountain belt. Alternatively, the low μ of 0.002 may infer that the Wutai and Jiashian earthquakes had just released a small portion instead of all shear stresses applied on the fault planes. We speculate that other major faults with different geometries in Tainan and Kaohsiung region which are located west of the Wutai area (Fig. 1) may support substantial differential stress in the lithosphere as well. Therefore, the stress drop can be much higher than that released by a single earthquake like Wutai. Applying a larger stress drop to the Eq. (7) can consequently bring the coefficient of friction much closer to the upper bound value of 0.03.

Investigations of the coefficient of friction on faults have been conducted for the Taiwan area using a variety of methods. Suppe (2007) inferred the effective friction coefficient ranging from 0.04–0.1 on the basal detachment beneath Taiwan mountain belt from the covariation of surface slope with detachment dip. Hsu et al. (2009) estimated μ of 0.01 based on the coseismic stress drop of the 1999 Chi–Chi earthquake and the rotation of the principal stress axes. Tanaka et al. (2006) used the thermal anomalies measured on the Chelungpu fault to infer a low friction coefficient of 0.04–0.24. These estimates constrained by various observations and techniques generally agree with our derived upper-bound value of 0.03.

Normal- and thrust-faulting earthquakes prevail in the upper and lower curst beneath the southern Central Range where the Eurasian plate underthrusts the Philippine Sea plate (Fig. 8), and the evident transition of normal- to thrust-events at depths of 10–15 km (Fig. 8c) provides constraints on the rheology of lithosphere in southern Taiwan. Using $\mu = 0.03$ from the crustal thickness contrasts, we propose a rheological model as shown in Fig. 9b. The slopes of solid lines are constrained by μ in both extensional and compressional stress regime, and the rheology of the upper mantle is estimated based on the power-law dislocation creep of olivine governed by $\Delta\sigma = (\varepsilon / A^*)^{1/n}\exp(H / nRT)$, where n is the stress component, A^* is material constant, H is activation enthalpy, $R = 8.314\,\mathrm{J\,mol^{-1}\,K^{-1}}$ is the gas constant, and T is the absolute temperature. We use the parameters of dislocation creep proposed for general

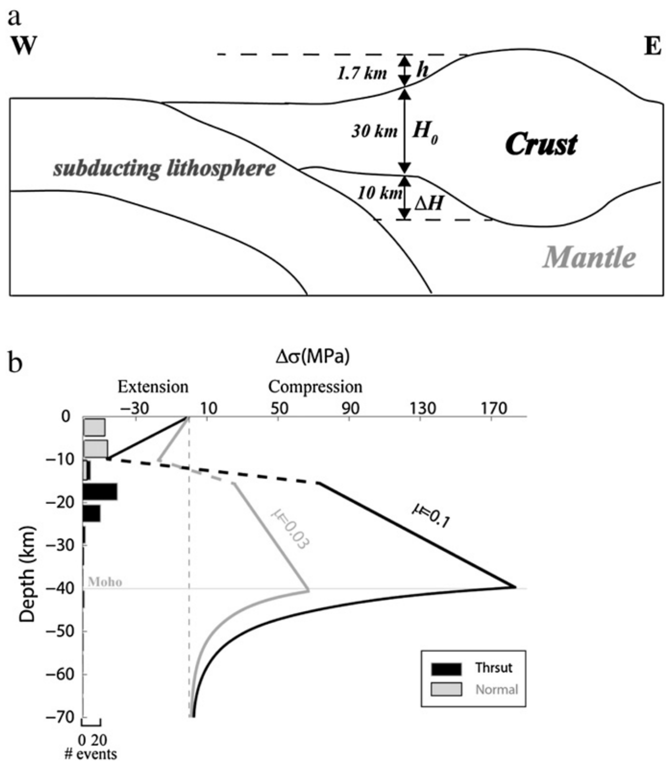

Fig. 9. (a) Schematic diagram showing the E–W profile of the mountain belt in southern Taiwan. Parameters used to calculate the average horizontal compressive force in this study include the density of the crust ρ_c; the mountain elevation h; the crustal thickness H_0, and the thickness of the crustal root ΔH (Kuo-Chen et al., 2012a). (b) The distribution of differential stress with depth. The straight solid lines indicate stresses in the brittle regime with $\mu = 0.03$ inferred in this study and $\mu = 0.1$ for reference. The curved solid lines show the differential stress in the mantle and are calculated by using the olivine dislocation creep and geotherm of the Eurasian continental lithosphere. The histogram on the left shows the distribution of different types of focal mechanism at depths.

lithosphere rocks (Goetze and Poirier, 1978; Hansen and Carter, 1982; Wilks and Carter, 1990), and the geotherm of the Eurasian continental lithosphere (Mouthereau and Petit, 2003). The average strain rate across the mountain belt is about $3–5 \times 10^{-15}$ s^{-1} (Seno et al., 1993; Yu et al., 1997), and we use rates ranged from 10^{-13} to 10^{-15} s^{-1} to obtain the required plastic failure curves in the mantle. The lithospheric rheology shown in Fig. 9b provides a working model for the distribution of differential stress with depth, which can be applied to future geodynamic studies in southern Taiwan.

6. Conclusions

Using GPS coseismic displacements and an elastic half-space dislocation model, we infer that the Wutai earthquake experienced a reverse slip of 28–112 mm and a left-lateral slip of 9–45 mm, with a maximum slip of 121 mm occurred in the west of the epicenter at a depth range of 20–25 km. The rupture area is characterized by a NE–SW compressional stress as evidenced by the cleavage orientations and the interpretations of stress tensor inversions from earthquake focal mechanisms. We use the stress drops of the Wutai and Jiashian earthquakes as well as the crustal thickness contrasts to estimate the coefficient of friction on fault planes. A very low value of 0.002 for the Wutai rupture implies that other faults systems in this region may support substantial differential stress in the mountain belt. According to the distribution of normal- and thrust-faulting events at depths and the estimates of friction coefficient, we propose a lithospheric rheology model beneath the southern Central Range in Taiwan.

Acknowledgments

We thank the editor, Jean-Philippe Avouac and an anonymous reviewer for their thoughtful reviews and valuable comments that helped to improve the manuscript. We also have benefited from discussions with Louis Teng and Alex Copley. We are grateful to many colleagues at the Institute of Earth Sciences, Academia Sinica, who have participated in collecting continuous GPS data. The generous provision of continuous GPS data from the Central Weather Bureau, Central Geological Survey, and Ministry of the Interior, Taiwan, and the international GNSS Service community is appreciated. GMT was used to create several figures (Wessel and Smith, 1998). This research is supported by the Institute of Earth Sciences, Academia Sinica, IESAS1945, and the National Science Council of Taiwan grant NSC 101-2116-M-001-026-MY3 (Wessel and Smith, 1998).

References

Angelier, J., Colletta, B., Anderson, R.E., 1985. Neogene paleostress changes in the Basin and Range: a case study at Hoover Dam, Nevada–Arizona. Geol. Soc. Am. Bull. 96, 347–361. http://dx.doi.org/10.1130/0016-7606(1985)96<347:NPCITB>2.0.CO;2.

Blewitt, G., Lavallée, D., 2002. Effect of annual signals on geodetic velocity. J. Geophys. Res. 107, B72145. http://dx.doi.org/10.1029/2001JB000570.

Chan, C.H., Wu, Y.M., 2012. A seismicity burst following the 2010 M6. 4 Jiashian earthquake — implications for short-term seismic hazards in southern Taiwan. J. Asian Earth Sci. 59, 231–239. http://dx.doi.org/10.1016/j.jseaes.2012.08.011.

Copley, A., Avouac, J.P., Hollingsworth, J., Leprince, S., 2011. The 2001 Mw 7.6 Bhuj earthquake, low fault friction, and the crustal support of plate driving forces in India. J. Geophys. Res. 116, B08405. http://dx.doi.org/10.1029/2010JB008137.

Dong, D., Fang, P., Bock, Y., Cheng, M., Miyazaki, S., 2002. Anatomy of apparent seasonal variations from GPS-derived site position time series. J. Geophys. Res. 107. http://dx.doi.org/10.1029/2001JB000573 (ETG-9).

Goetze, C., Poirier, J., 1978. The mechanisms of creep in olivine. Philos. Trans. R. Soc. Lond., B 288, 99–119.

Hansen, F.D., Carter, N.L., 1982. Creep of selected crustal rocks at 1000 MPa. Eos Trans. AGU 63, 437.

Harris, R.A., Segall, P., 1987. Detection of a locked zone at depth on the Parkfield, California, segment of the San-Andreas Fault. J. Geophys. Res. 92, 7945–7962. http://dx.doi.org/10.1029/JB092iB08p07945.

Hsieh, M.C., Zhao, L., Ma, K.F., 2014. Efficient waveform inversion for average earthquake rupture in three-dimensional structures. Geophys. J. Int. 198, 1279–1292. http://dx.doi.org/10.1093/gji/ggu209.

Hsu, Y.J., Avouac, J.P., Yu, S.B., Chan, C.H., Wu, Y.M., Woessner, J., 2009. Spatio-temporal slip, and stress level on the faults within the western foothills of Taiwan: implications for fault frictional properties. Pure Appl. Geophys. 166, 1853–1884. http://dx.doi.org/10.1111/j.1365-246X.2010.04609.x.

Hsu, Y.J., Yu, S.B., Kuo, L.C., Tsai, Y.C., Chen, H.Y., 2011. Coseismic deformation of the 2010 Jiashian, Taiwan earthquake and implications for fault activities in southwestern Taiwan. Tectonophysics 502, 328–335. http://dx.doi.org/10.1016/j.tecto.2011.02.005.

Hu, J.C., Angelier, J., 2004. Stress permutations: three-dimensional distinct element analysis accounts for a common phenomenon in brittle tectonics. J. Geophys. Res. 109, B09403. http://dx.doi.org/10.1029/2003JB002616.

Kuo-Chen, H., Wu, F.T., Roecker, S.W., 2012a. Three-dimensional P velocity structures of the lithosphere beneath Taiwan from the analysis of TAIGER and related seismic data sets. J. Geophys. Res. 117. http://dx.doi.org/10.1029/2011JB009108.

Kuo-Chen, H., Wu, F.T., Jenkins, D.M., Mechie, J., Roecker, S.W., Wang, C.-Y., Huang, B.-S., 2012b. Seismic evidence for the α–β quartz transition beneath Taiwan from Vp/Vs tomography. Geophys. Res. Lett. 39, L22302. http://dx.doi.org/10.1029/2012GL053649.

Lee, S.J., Mozziconacci, L., Liang, W.T., Hsu, Y.J., Huang, W.G., Huang, B.S., 2013. Source complexity of the 4 March 2010 Jiashian, Taiwan, Earthquake determined by joint inversion of teleseismic and near field data. J. Asian Earth Sci. 64, 14–26. http://dx.doi.org/10.1016/j.jseaes.2012.11.018.

Lewis, C., Chen, S.W., Yen, P.C., 2004. Magnetic surveying of the Chaochou fault of southern Taiwan: culmination of basement-involved surface thrusting in arc–continent collision. Int. Geol. Rev. 46, 399–408. http://dx.doi.org/10.2747/0020-6814.46.5.399.

Lin, A.T., Watts, A.B., 2002. Origin of the West Taiwan basin by orogenic loading and flexure of a rifted continental margin. J. Geophys. Res. 107, B9218. http://dx.doi.org/10.1029/2001JB000669.

Madariaga, R., 1979. On the relation between seismic moment and stress drop in the presence of stress and strength heterogeneity. J. Geophys. Res. 84, 2243–2250.

Molnar, P., Lyon-Caen, H., 1988. Some simple physical aspects of the support, structure, and evolution of mountain belts. Geol. Soc. Am. Spec. Pap. 218, 179–208.

Mouthereau, F., Petit, C., 2003. Rheology and strength of the Eurasian continental lithosphere in the foreland of the Taiwan collision belt: constraints from seismicity, flexure, and structural styles. J. Geophys. Res. 108, B112512. http://dx.doi.org/10.1029/2002JB002098.

Nikolaidis, R., 2002. Observation of Geodetic and Seismic Deformation with the Global Positioning System, Earth Sciences. University of California, San Diego, p. 249.

Okada, Y., 1985. Surface deformation due to shear and tensile faults in a half-space. Bull. Seismol. Soc. Am. 75, 1135–1154.

Rau, R.J., Lee, J.C., Ching, K.E., Lee, Y.H., Byrne, T.B., Chen, R.Y., 2012. Subduction–continent collision in southwestern Taiwan and the 2010 Jiashian earthquake sequence. Tectonophysics 578, 107–116. http://dx.doi.org/10.1016/j.tecto.2011.09.013.

Seno, T., Stein, S., Gripp, A.E., 1993. A model for the motion of the Philippine Sea plate consistent with Nuvel-1 and geological data. J. Geophys. Res. 98, 17941–17948.

Suppe, J., 2007. Absolute fault and crustal strength from wedge tapers. Geology 35, 1127–1130. http://dx.doi.org/10.1130/g24053a.1.

Tanaka, H., Chen, W.M., Wang, C.Y., Ma, K.F., Urata, N., Mori, J., Ando, M., 2006. Frictional heat from faulting of the 1999 Chi–Chi, Taiwan earthquake. Geophys. Res. Lett. 33, L16316. http://dx.doi.org/10.1029/2006gl026673.

Turcotte, D.L., Schubert, G., 2002. Geodynamics. 2nd ed. Cambridge University Press, Cambridge. U. K.

van Dam, T., Wahr, J., Milly, P., Shmakin, A., Blewitt, G., Lavallée, D., Larson, K., 2001. Crustal displacements due to continental water loading. Geophys. Res. Lett. 28, 651–654. http://dx.doi.org/10.1029/2000GL012120.

Wessel, P., Smith, W.H., 1998. New, improved version of Generic Mapping Tools released. Eos Trans. AGU 79 (47), 579.

Wilks, K.R., Carter, N.L., 1990. Rheology of some continental lower crustal rocks. Tectonophysics 182, 57–77.

Williams, S.D.P., 2003. Offsets in global positioning system time series. J. Geophys. Res. 108, B62310. http://dx.doi.org/10.1029/2002JB002156.

Wiltschko, D.V., Hassler, L., Hung, J.H., Liao, H.S., 2010. From accretion to collision: motion and evolution of the Chaochou Fault, southern Taiwan. Tectonics 29, TC2015. http://dx.doi.org/10.1029/2008TC002398.

Wu, Y.M., Zhao, L., Chang, C.H., Hsu, Y.J., 2008. Focal-mechanism determination in Taiwan by genetic algorithm. Bull. Seismol. Soc. Am. 98, 651–661. http://dx.doi.org/10.1785/0120070115.

Wu, Y.M., Chang, C.H., Kuo-Chen, H., Huang, H.H., Wang, C.Y., 2013. On the use of explosion records for examining earthquake location uncertainty in Taiwan. Terr. Atmos. Ocean. Sci. 24, 685–694. http://dx.doi.org/10.3319/TAO.2013.01.31.01(T).

Yu, S.B., Chen, H.Y., Kuo, L.C., 1997. Velocity field of GPS stations in the Taiwan area. Tectonophysics 274, 41–59. http://dx.doi.org/10.1016/S0040-1951(96)00297-1.